# Thermally Induced Domain Migration and Interfacial Restructuring in Cation Exchanged ZnS-Cu<sub>1.8</sub>S Heterostructured Nanorods

Haley L. Young, <sup>1</sup> Enrique D. Gomez, <sup>2,3,4</sup> and Raymond E. Schaak <sup>1,2,4,\*</sup>

E-mail: res20@psu.edu

## **ABSTRACT**

Partial cation exchange reactions can be used to rationally design and synthesize heterostructured nanoparticles that are useful targets for applications in photocatalysis, nanophotonics, thermoelectrics, and medicine. Such reactions introduce intraparticle frameworks that define the spatial arrangements of different materials within a heterostructured nanoparticle, as well as the orientations and locations of their interfaces. Here, we show that upon heating to temperatures relevant to their synthesis and applications, the ZnS regions and Cu<sub>1.8</sub>S/ZnS interfaces of heterostructured ZnS-Cu<sub>1.8</sub>S nanorods migrate and restructure. We first use partial cation exchange reactions to synthesize a library of seven distinct samples containing various patches, bands, and tips of ZnS embedded within Cu<sub>1.8</sub>S nanorods. Upon annealing in solution or in air, ex situ TEM analysis shows evidence that the ZnS domains migrate in different ways, depending upon their sizes and locations. Using differential scanning calorimetry, we correlate the threshold temperature for ZnS migration to the superionic transition temperature of Cu<sub>1.8</sub>S, which facilitates rapid diffusion throughout the nanorods. We then use *in situ* thermal TEM to study the evolution of individual ZnS-Cu<sub>1.8</sub>S nanorods upon heating. We find that ZnS domain migration occurs through a ripening process that minimizes small patches with higher-energy interfaces in favor of larger bands and tips having lower-energy interfaces, as well as through restructuring of higherenergy Cu<sub>1.8</sub>S/ZnS interfaces. Notably, Cu<sub>1.8</sub>S nanorods containing multiple patches of ZnS thermally transform into ZnS-Cu<sub>1.8</sub>S heterostructured nanorods having ZnS tips and/or central bands, which provides mechanistic insights into how these commonly observed products form during synthesis.

<sup>&</sup>lt;sup>1</sup> Department of Chemistry, <sup>2</sup> Department of Chemical Engineering, <sup>3</sup> Department of Materials Science and Engineering, and <sup>4</sup> Materials Research Institute, The Pennsylvania State University, University Park, Pennsylvania 16802, United States

## INTRODUCTION

Heterostructured nanoparticles integrate two or more distinct materials, and this integration combines the properties of each individual component and/or allows new properties to emerge through synergistic interactions. <sup>1,2</sup> For example, three component, double-heterojunction nanorods containing CdS, CdSe, and ZnSe have been synthesized to enable both light-detection and emission for applications in advanced displays.<sup>3</sup> Dual-plasmonic heterostructures such as Au@Cu<sub>2-x</sub>Se with high optical absorption and photothermal conversion are promising for use as photothermal agents in cancer treatment.<sup>4</sup> Among the methods available for synthesizing heterostructured nanoparticles, cation exchange reactions are particularly powerful.<sup>1,5</sup> In these reactions, one type of cation in a nanoparticle is replaced by another from solution to modify composition, but morphology and crystal structure are often retained.<sup>6</sup> Heterostructured nanoparticles can form when cation exchange is purposely incomplete, resulting in the coexistence of multiple segregated phases connected through internal interfaces.<sup>7–9</sup> Multiple partial cation exchange reactions can be applied sequentially to produce scalable libraries and megalibraries of complex heterostructured nanoparticles containing several distinct materials in precise locations within the particle. <sup>10,11</sup> Such particles include useful targets for optical and biological barcodes, as well as for photocatalytic, thermoelectric, and optoelectronic applications.<sup>3,12,13</sup>

Heterostructured nanoparticles are often synthesized at elevated temperatures, ranging from tens to hundreds of degrees Celsius.<sup>14</sup> Annealing heterostructured nanoparticles to higher temperatures can facilitate diffusion, which can result in changes to the crystal structure, morphology, and spatial distribution of elements.<sup>15–17</sup> For example, supported core-shell nanoparticles have been shown to transform into high entropy alloys upon annealing.<sup>18,19</sup> Annealing also was used to determine that surface and interfacial energies played a prominent role in defining the thermodynamically preferred architectures of polyelemental nanoparticles.<sup>14,20</sup> In addition to these synthetic considerations, many of the existing and envisioned applications of heterostructured nanoparticles either require or generate heat, or they are potentially impacted by external temperature fluctuations. For example, light absorption by nanostructured photothermal materials causes a temperature increase that can range from tens to hundreds of degrees.<sup>21–24</sup> Likewise, applying a voltage to nanostructured thermoelectric composites induces a temperature gradient, or application of a temperature gradient induces a potential difference across the material.<sup>25–28</sup> For these reasons, it is important to identify and understand thermally induced changes in heterostructured nanoparticles at temperatures that are relevant to both synthesis and applications.

Here, we probe the temperature-dependent stability of heterostructured nanorods containing patches of ZnS embedded in different ways within nanorods of roxbyite copper sulfide, Cu<sub>1.8</sub>S. The patchy ZnS–Cu<sub>1.8</sub>S nanorods, synthesized by partially exchanging the Cu<sup>+</sup> cations in roxbyite with Zn<sup>2+</sup>, represent an ideal model system for interrogating how temperature influences nanostructural features. Synthetic access to a library of seven distinct ZnS–Cu<sub>1.8</sub>S variants having different numbers of ZnS domains within Cu<sub>1.8</sub>S nanorods of identical shape and size allows us to identify and deconvolute the roles of domain location, size, and interface on thermal evolution. By annealing the heterostructured ZnS–Cu<sub>1.8</sub>S nanorods in solution, we find evidence of thermally induced ZnS domain migration that appears to be dependent upon domain size and location. We then anneal the ZnS–Cu<sub>1.8</sub>S nanorods in air to further interrogate their thermal evolution. We also use *in situ* thermal TEM to analyze the temperature dependent ZnS domain migration, at the single

particle level, to precisely correlate the observed thermal evolution with the key characteristics of the ZnS domains. These studies provide *ex situ* and *in situ* glimpses into the ways in which cation exchanged heterostructured nanoparticles evolve with temperature. Additionally, the results provide mechanistic insights into the ways in which various types of previously reported heterostructured nanoparticles may form, <sup>10,29</sup> as well as design guidelines for synthetically manipulating them to generate heterostructured nanoparticles that are not readily accessible using existing knowledge.

## **RESULTS AND DISCUSSION**

Partial exchange of the  $Cu^+$  cations in roxbyite  $Cu_{1.8}S$  nanorods with  $Zn^{2+}$  in the presence of trioctylphosphine (TOP) provides access to a library of seven distinct heterostructured  $ZnS-Cu_{1.8}S$  nanorod products by manipulating reaction temperature and reagent concentration. These  $ZnS-Cu_{1.8}S$  nanorods allow us to interrogate the thermal evolution of multiple distinct types of ZnS inclusions that span a range of sizes, locations, and interfaces, all of which are anticipated to influence temperature-dependent behavior.

## Formation and Interface Structure of ZnS-Cu<sub>1.8</sub>S Nanorods

Figure 1 shows HAADF-STEM images for each of the heterostructured ZnS-Cu<sub>1.8</sub>S nanorods that were synthetically accessible, along with brief summaries of the protocols used to make them. Stoichiometry-limited partial cation exchange reactions<sup>29</sup> using ZnCl<sub>2</sub> produced single-tip ZnS-Cu<sub>1.8</sub>S nanorods by heating at 120 °C for 30 minutes, central band Cu<sub>1.8</sub>S–ZnS–Cu<sub>1.8</sub>S nanorods by ramping from room temperature to 100 °C and heating for 30 minutes, and a mixed population of single-tip, central band, and double-tip ZnS-Cu<sub>1.8</sub>S nanorods by holding the reaction at 50 °C for 1 hour and then ramping to 160 °C and heating for 30 minutes. The small substoichiometric amount of Zn<sup>2+</sup>, combined with the reaction conditions, limit the number of sites at which cation exchange initiates and propagates. 10,30 Time-limited partial cation exchange reactions, using a twofold excess ZnCl<sub>2</sub> at 50 °C and stopping the reaction before completion, provides a higher concentration of Zn<sup>2+</sup> that allows cation exchange to initiate and propagate simultaneously at multiple locations of the nanorod. 11 Such reactions yield Cu<sub>1.8</sub>S nanorods with patches of ZnS throughout, which we refer to collectively as patchy ZnS-Cu<sub>1.8</sub>S nanorods. The average sizes of the ZnS patches could be controlled by altering the reaction time from 45 minutes to 1.5 hours. Samples containing primarily single-patch and double-patch ZnS-Cu<sub>1.8</sub>S nanorods were synthesized using modified heating profiles. The single patch particles were synthesized using a variant of the procedure used to make the central band nanorods<sup>10</sup>; the Cu<sub>1.8</sub>S particles were injected into the cation exchange solution at room temperature and ramping the temperature to 90 °C before immediately quenching with an ice bath. While the majority product had a central ZnS patch along the length of the nanorod, some single tipped rods formed as well. Similarly, the double patch particles were synthesized by injecting the Cu<sub>1.8</sub>S particles at 50 °C and ramping the temperature up to 80 °C to hold for three minutes. The double patch particles can be categorized as having two central ZnS patches along the length of the rod, a ZnS domain at both tips, or having one central ZnS patch as well as one ZnS tip.

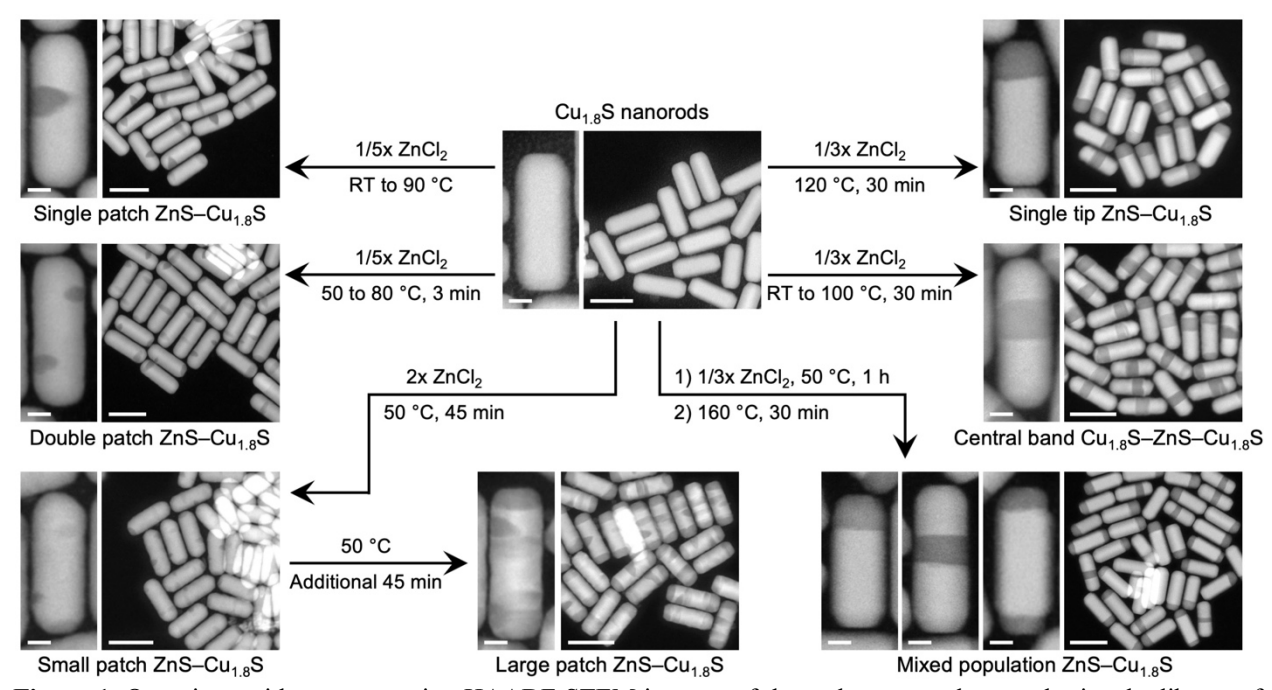


**Figure 1.** Overview, with accompanying HAADF-STEM images, of the pathways used to synthesize the library of heterostructured ZnS/Cu<sub>1.8</sub>S nanorods from Cu<sub>1.8</sub>S that are used in this study. In the HAADF-STEM images, darker contrast regions correspond to ZnS and lighter contrast regions correspond to Cu<sub>1.8</sub>S. Scale bars for the full images are 50 nm and for the cropped particles are 10 nm.

The crystal structures of roxbyite Cu<sub>1.8</sub>S and wurtzite ZnS, showing only the anions, are included in Figure 2a.<sup>31,32</sup> Roxbyite adopts a distorted hexagonal close packed (hcp) anion structure, while the anion structure of wurtzite is hcp. Nanorods of roxbyite Cu<sub>1.8</sub>S are known to form single-domain crystals with the distorted close packed planes stacking along the long-axis direction of the nanorods.<sup>31,33</sup> The formation of these particular interfaces during partial cation exchange is generally understood to arise from a combination of the immiscibility of Cu<sub>1.8</sub>S and ZnS, which leads to phase segregation, and the minimization of both the number of interfaces between the phases and the interfacial energies, which leads to interfacing the crystal planes that have the best lattice match.<sup>34,35</sup>

The most commonly observed interface between Cu<sub>1.8</sub>S and ZnS, which has the best lattice match and therefore minimizes strain and interfacial energy, is along this direction (Figure 2a) and corresponds to interfacing of the close packed planes, *i.e.*, Cu<sub>1.8</sub>S (100) and ZnS (001).<sup>10,36</sup> The perpendicular (010) Cu<sub>1.8</sub>S and (100) ZnS planes have a much larger difference in their lattice spacings and therefore it is very uncommon to see these two families of planes interfaced with each other.<sup>10</sup> The high-resolution TEM (HRTEM) images of the single tipped and double patch nanorods in Figures 2b and 2c provide visualization of the interfaces between the Cu<sub>1.8</sub>S and ZnS regions. In the single tipped nanorod, the ZnS domain penetrates the width of the nanorod and the materials share the favored interface along the close packed planes. The experimentally measured spacing of the (400) plane of Cu<sub>1.8</sub>S, which corresponds to the close packed planes, was 3.4 Å, which matches well with the value of 3.35 Å that is expected based on the crystal structure.<sup>31</sup> For ZnS, the experimentally measured spacing of the (002) close packed plane was 3.2 Å, which also agrees well with the expected value of 3.11 Å.<sup>32</sup>

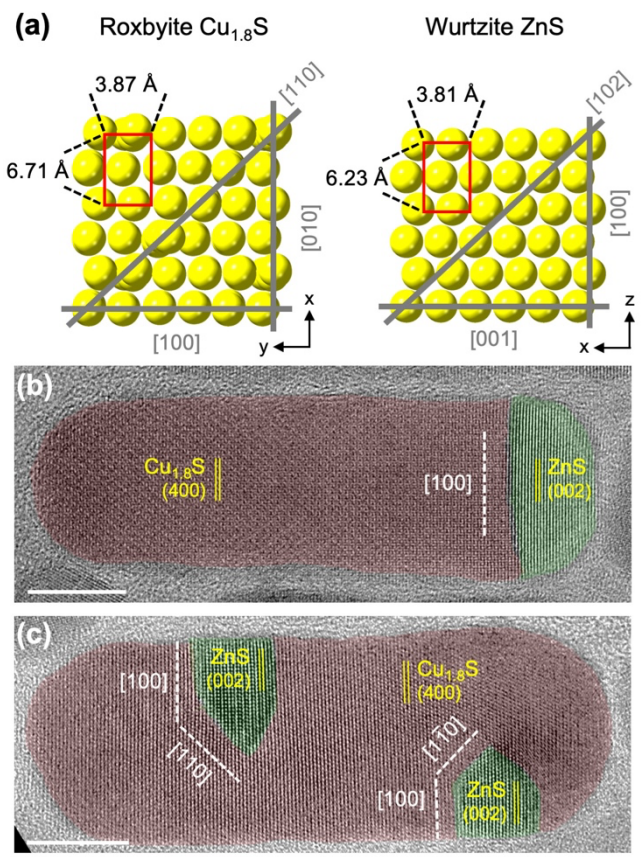


**Figure 2.** (a) The crystal structures of roxbyite Cu<sub>1.8</sub>S and wurtzite ZnS, showing only the sulfur anions (yellow) to highlight the similarities between their structures. Key crystallographic planes, as well as unit cell dimensions, are denoted. The HRTEM images of the (b) single tipped and (c) double patched heterostructures are false-colored (red for Cu<sub>1.8</sub>S and green for ZnS) to highlight the differences in the Cu<sub>1.8</sub>S/ZnS interfaces. The white dashed lines show the crystallographic directions in which the Cu<sub>1.8</sub>S interfaces with the ZnS regions. Scale bars are 50 nm.

In the double patched nanorods in Figure 2c, the spacings of the (002) planes of ZnS and the (400) planes of Cu<sub>1.8</sub>S were measured to be 3.2 Å and 3.4 Å, respectively. The ZnS domains within these nanorods are patches that do not fully penetrate through the nanorod like the ZnS domains in the single tipped nanorods did, and as a result, interfaces other than the preferred ZnS(001)/Cu<sub>1.8</sub>S(100) can be seen. Near the edge of the double patched nanorods, the ZnS domains appear to align with the close packed plane, corresponding to the preferred ZnS(001)/Cu<sub>1.8</sub>S(100) interface. However, as the ZnS patches approach the center of the nanorod, they begin to taper to a rounded point; other less-preferred interfaces that have a larger lattice mismatch must be present to accommodate this tapering. The angle between the tapered patch edge and the (100) planes of Cu<sub>1.8</sub>S is measured to be approximately 45°, which matches best with an interface composed of the (110) planes of Cu<sub>1.8</sub>S, with an actual angle to the close packed plane of 45°, and the (102) planes of ZnS, with an actual angle to the close packed plane of 43°. While this interface is not as favorable as the Cu<sub>1.8</sub>S(100)/ZnS(001) interface shown in the single tipped rod based on lattice matching and interfacial energy considerations, it has been documented before and is more favorable than the Cu<sub>1.8</sub>S(010)/ZnS(100) interface.<sup>11</sup>

# Ex Situ Annealing of ZnS-Cu<sub>1.8</sub>S Nanorods

We began studying the thermal evolution of heterostructuring in the patchy ZnS–Cu<sub>1.8</sub>S nanorods by heating them in solution. To do so, we dispersed the large patched ZnS–Cu<sub>1.8</sub>S nanorods in octadecene and injected them into a mixture of octadecene and oleylamine preheated to 110 °C and allowed them to anneal for 1 hour. HAADF-STEM images for the particles before and after annealing are shown in Figure 3a; the darker contrast regions are ZnS while the lighter contrast regions are Cu<sub>1.8</sub>S. Several nanorods show some residual patches along the body, but the majority show the ZnS congregated at the tips, making double tipped ZnS–Cu<sub>1.8</sub>S nanorods.

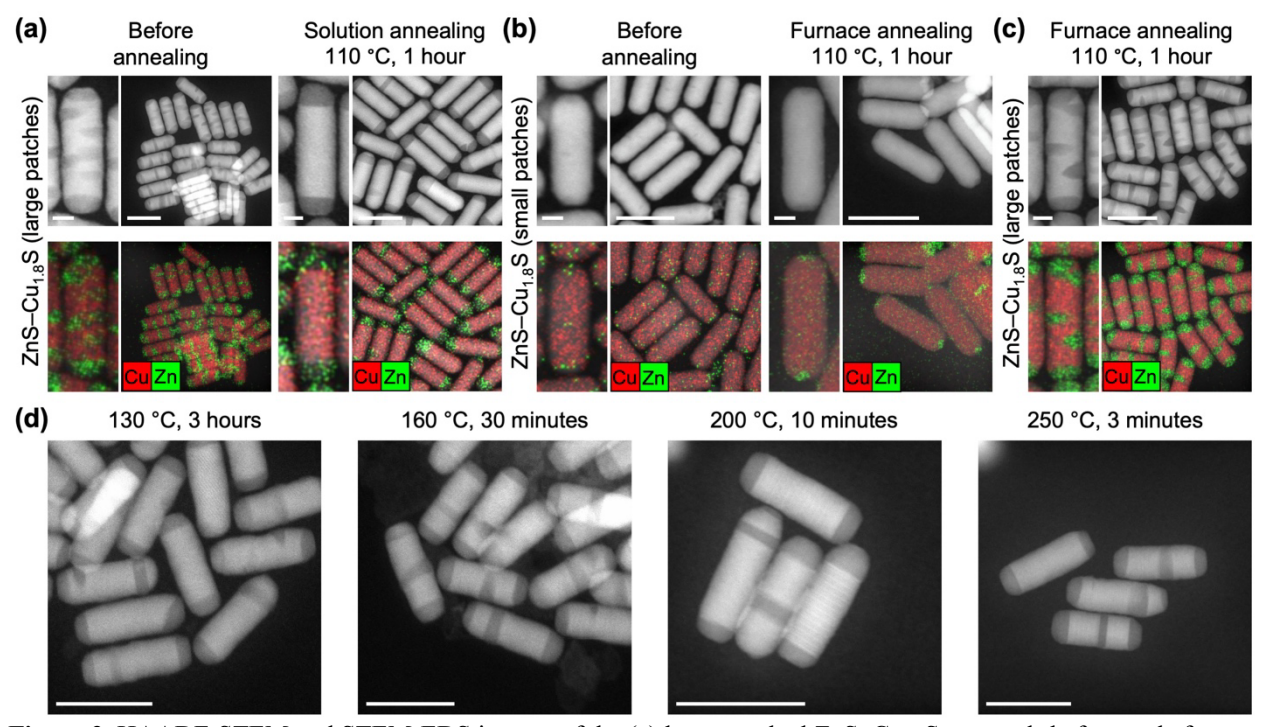


**Figure 3.** HAADF-STEM and STEM-EDS images of the (a) large patched ZnS–Cu<sub>1.8</sub>S nanorods before and after annealing in solution at 110  $^{\circ}$ C for 1 hour, (b) small patched ZnS–Cu<sub>1.8</sub>S nanorods before and after annealing in a box furnace at 110  $^{\circ}$ C for 1 hour, and (c) large patched ZnS–Cu<sub>1.8</sub>S nanorods after annealing in a box furnace at 110  $^{\circ}$ C for 1 hour. (d) HAADF–STEM images of the patchy ZnS–Cu<sub>1.8</sub>S nanorods after annealing in a box furnace at the temperatures and times indicated. Scale bars are for the cropped nanorods in (a-c) are 10 nm and scale bars for the full images in (a-d) are 50 nm.

Given the coalescence of ZnS domains that was observed upon solution annealing of the large patchy particles, we next carried out several *ex-situ* annealing experiments. Initially, we deposited two distinct types of patchy ZnS–Cu<sub>1.8</sub>S nanorods onto silicon wafers and annealed them in air in a box furnace at 110 °C for 1 hour (Figure 3b), which is analogous to that of the solution annealing experiment. The first type of patchy ZnS–Cu<sub>1.8</sub>S nanorods contained small domains of ZnS embedded within the Cu<sub>1.8</sub>S nanorods, and upon annealing, these domains appeared to exhibit the same coalescence of ZnS at the tips of the nanorods that was observed during solution annealing. Before annealing, the patches of ZnS are too small to be visualized by the STEM-EDS element maps. However, the darker contrast of the ZnS regions, relative to Cu<sub>1.8</sub>S, can be seen clearly in HAADF images. After annealing, the larger coalesced domains at the tips are clearly seen in the HAADF image, as well as by EDS. In contrast, annealed under the same conditions, the second

type of patchy ZnS–Cu<sub>1.8</sub>S nanorods that contained large domains of ZnS embedded within the Cu<sub>1.8</sub>S nanorods did not show significant coalescence (Figure 3c). Instead, the ZnS domains remained distributed throughout the body of the nanorod. Full STEM-EDS element maps are shown in Figure S1. By comparing the results from Figure 3a to 3c, the method by which the nanorods were heated appears to influence the degree to which the patches coalesce, which is not unexpected. We suspect that solution-phase annealing in an environment containing surfactants such as oleylamine, as well as an environment where the particles are dispersed and non-interacting, helps to accelerate patch migration compared to annealing dried samples in a box furnace.

Because the ZnS domains in the small-patch ZnS-Cu<sub>1.8</sub>S nanorods migrated upon heating at 110 °C for 1 hour but those in the large-patch rods did not, we briefly explored higher-temperature annealing. We hypothesized that higher temperatures would facilitate migration, such that shorter times would be required. Rather than map out all possible combinations of temperature and time at this stage, we selectively chose four sets of conditions to initially explore how the large-patch ZnS-Cu<sub>1.8</sub>S nanorods evolved upon annealing on Si wafers in air in a box furnace at increasing temperatures and decreasing times. The HAADF-STEM images in Figure 3d show that higher temperatures are effective at inducing domain migration, generally concentrating the ZnS at the tips of the nanorods. When heated at 130 °C for 3 hours, the nanorods have ZnS at the tips and some also have one or two patches along the body of the nanorod. Similar results are seen for the nanorods annealed at 160 °C for 30 minutes, in addition to several central bands of ZnS nearly penetrating the width of the nanorods. Central bands that penetrate the width of the nanorod have a characteristically consistent contrast through the entire ZnS domain. Bands that appear to have a gradient from darker to lighter contrast are assumed to be angled and therefore do not penetrate through the full width of the particle. Annealing at 200 °C for 10 minutes and 250 °C for 3 minutes resulted in particles with two or three well-defined domains of ZnS at the tips or as a central band. These ZnS domains exclusively span the width of the nanoparticle and interface with Cu<sub>1.8</sub>S along the close-packed (100) plane.

The data in Figure 3 point to the conclusion that post-synthetic annealing of the patchy ZnS–Cu<sub>1.8</sub>S nanorods can induce migration of the ZnS domains, causing them to coalesce and therefore decrease the number of interfaces between ZnS and Cu<sub>1.8</sub>S. However, the data also indicate that this behavior is dependent on temperature, time, and the size of the patches, as smaller ZnS patches migrate at lower temperatures while larger ZnS patches require higher temperatures and/or longer annealing times to do so. While the experiments in Figure 3 provide insights into thermal behavior of the ZnS domains in Cu<sub>1.8</sub>S, they do not provide direct comparison of the same particles before and after annealing. To better understand this temperature dependent behavior, we moved to depositing the patchy ZnS–Cu<sub>1.8</sub>S nanorods on TEM finder grids that contain labeled grid squares. These grids allow us to find and analyze a group of particles by TEM before annealing and then remove the sample to anneal the particles on the grid in a box furnace. We can then find the exact same group of particles for further analysis after annealing, and track thermally induced changes for individual particles.

Figure 4 shows HAADF-STEM images of the same large-patch ZnS-Cu<sub>1.8</sub>S particles assynthesized and after annealing at 250 °C for 3 minutes on a TEM finder grid in a box furnace in air. As discussed before, the patchy ZnS-Cu<sub>1.8</sub>S nanorods have multiple ZnS domains throughout

the body and at the tips. After annealing, the ZnS domains at the nanorod tips appear to remain in place. Additionally, they appear (based on qualitative observations) to grow slightly in size, become darker in contrast, and/or flatten at the interface to become perpendicular to the nanorod length; the flattened interface best aligns the close-packed planes of ZnS and Cu<sub>1.8</sub>S, as shown and discussed in Figure 1. As synthesized, many of the patchy nanorods have ZnS domains that span half (or less than half) of the width. After annealing, those ZnS domains are no longer present, likely migrating and contributing to the growth of the ZnS domains at the tips. In several of the nanorods, central bands appear after annealing. In some of these nanorods exhibiting central bands after annealing, a domain of ZnS was in that same location before annealing, typically spanning over half the nanorod width initially. In other central band nanorods after annealing, two smaller patches of ZnS appear to be positioned close together but originating from opposite sides of the nanorod; in these cases, the appearance of the central band is likely due to the patches merging together into a combined central band. Corresponding XRD patterns, shown in Figure 4 for assynthesized large-patch ZnS-Cu<sub>1.8</sub>S particles and after annealing at 250 °C for 3 minutes on a Si wafer, indicate that the phases that comprise the nanoparticles are conserved through the annealing process. In the XRD patterns, the most prominent peaks are due to Cu<sub>1.8</sub>S peaks, while the small crystallite sizes of the ZnS domains leads to broad XRD peaks that are observed as shoulders next to the Cu<sub>1.8</sub>S peaks; the most prominent wurtzite ZnS peaks in the experimental XRD patterns before and after annealing are at 27 degrees and just above 30 degrees. The composition, based on EDS analysis, also remains the same after annealing as it was prior to annealing, as shown by the Cu:Zn ratio plotted in Figure S2.

# Role of the Superionic Transition in Cu<sub>1.8</sub>S

Throughout all of the annealing reactions presented in Figures 3 and 4, the nanorod morphology does not change, and as shown in Figure S2, the Cu:Zn ratio remains constant. These observations suggest that the nanorod framework, which is Cu<sub>1.8</sub>S, remains intact while the Zn<sup>2+</sup> migrates through it. To better understand the rationale for this migration behavior, we considered the vacancy-rich nature of Cu<sub>1.8</sub>S, which makes it a useful template for cation exchange. Cu<sub>1.8</sub>S is known to be an ionic conductor where the Cu<sup>+</sup> cations can rapidly diffuse through it.<sup>37</sup> The vacancies in copper sulfide materials lend them to experience a superionic transition at a critical temperature of around 100 °C (Figure 5).<sup>37,38</sup> This superionic character gives Cu<sub>1.8</sub>S a very high ion conductance, making it a desirable material for use as a solid electrolyte in batteries. <sup>38,39</sup> Above the critical temperature, the copper cations are no longer locked into their crystallographic positions, but instead are free to move among all possible sites, which allows them to behave as a cationic liquid while the sulfur substructure remains intact. <sup>37,38,40</sup> Figure 5a shows DSC data for the roxbyite Cu<sub>1.8</sub>S nanorods; complete data, including an initial scan for conditioning and multiple additional scans to demonstrate reproducibility, are shown in Figure S3. The superionic transition of the Cu<sub>1.8</sub>S nanorods is 98 °C, which is slightly lower than the bulk superionic transition at ca. 103 °C. Many factors that influence the superionic transition temperature may play a role here, including crystallite size, vacancies, defects, and crystal phase.<sup>38</sup> Additionally, the onset of the phase change upon cooling is at a much lower temperature than upon heating; such hysteresis is common and is often an effect of superheating or subcooling. 38,41-43 Analogous DSC data for ZnS nanorods made by complete cation exchange of Cu<sub>1.8</sub>S (Figure 5b), and therefore that have the same morphology and size, do not show evidence of a superionic transition, as expected. However,

the DSC data for the patchy ZnS–Cu<sub>1.8</sub>S nanorods (Figure 5c) do show the superionic transition at 98 °C, which is attributed to the Cu<sub>1.8</sub>S component of the ZnS–Cu<sub>1.8</sub>S.

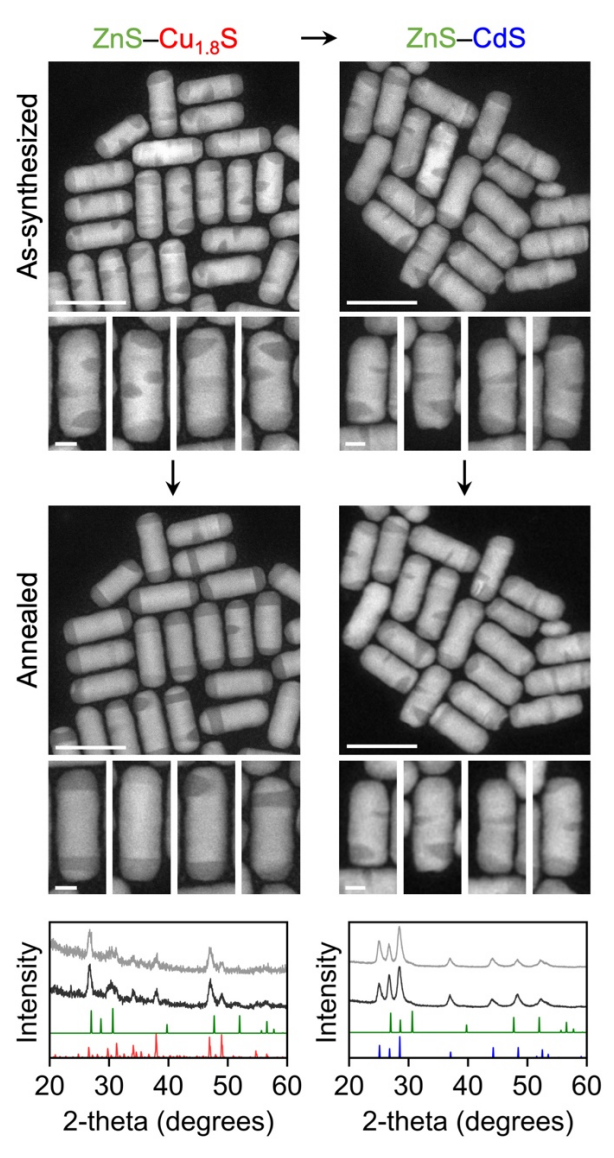


**Figure 4.** HAADF-STEM images and corresponding XRD data for the (left) as-synthesized patchy ZnS–Cu<sub>1.8</sub>S nanorods and (right) patchy ZnS–CdS nanorods made through cation exchange. Data are shown for the ZnS–Cu<sub>1.8</sub>S and ZnS–CdS nanorods both as-synthesized and annealed in a box furnace at 250 °C for 3 minutes using a finder TEM grid substrate. The XRD patterns show the ZnS–Cu<sub>1.8</sub>S and ZnS–CdS nanorods as–synthesized (black) and after annealing (grey), along with reference patterns for roxbyite (red), wurtzite ZnS (green), and wurtzite CdS (blue). Scale bars for the cropped nanorods are 10 nm and scale bars for full images are 50 nm.

The superionic transition in Cu<sub>1.8</sub>S occurred at 98 °C, which is slightly below the temperature of 110 °C where we first observed migration of the ZnS region in Figure 3. These observations and data therefore suggest that migration of the ZnS patches in ZnS–Cu<sub>1.8</sub>S nanorods may be facilitated by the superionic transition. Consistent with this hypothesis, we exchanged the Cu<sup>+</sup> cations in the patchy ZnS–Cu<sub>1.8</sub>S nanorods with Cd<sup>2+</sup> to form ZnS–CdS nanorods, which retain the ZnS patches but replace Cu<sub>1.8</sub>S with CdS. CdS does not exhibit a superionic transition, and indeed, annealing the patchy ZnS–CdS nanorods does not change the distribution of ZnS in CdS (Figure 4).

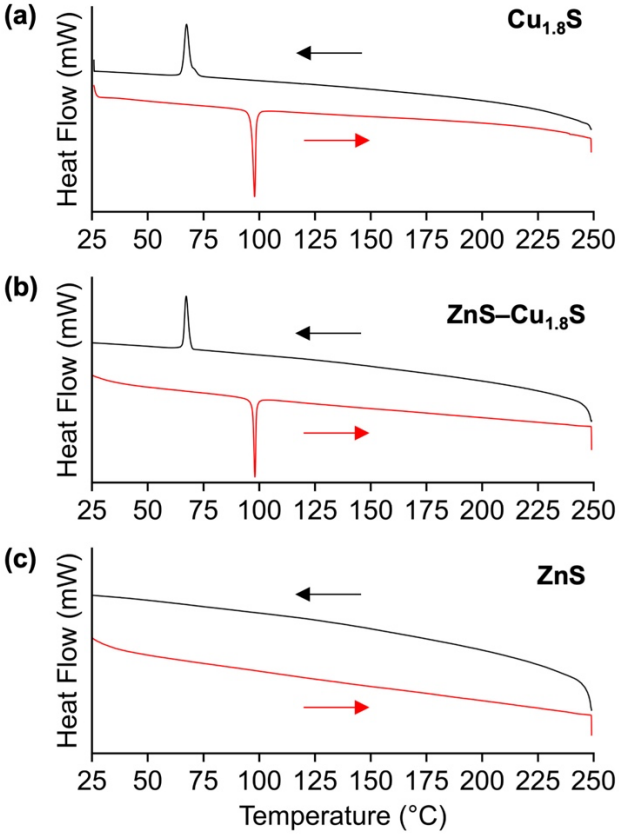


**Figure 5.** DSC data, plotted as heat flow vs temperature, showing the heating (red) and cooling (black) curves for (a)  $Cu_{1.8}S$  nanorods (b) patchy  $ZnS-Cu_{1.8}S$  nanorods, and (c) ZnS nanorods. The superionic transition for  $Cu_{1.8}S$  appears at 98 °C upon heating and is also observed in the patchy  $ZnS-Cu_{1.8}S$  nanorod sample, which also contains  $Cu_{1.8}S$ , but not in the ZnS sample.

## In Situ Annealing of ZnS-Cu<sub>1.8</sub>S Nanorods

All of the data presented so far indicate temperature-dependent migration of ZnS in patchy ZnS–Cu<sub>1.8</sub>S nanorods with a threshold temperature that correlates with that of the superionic transition in Cu<sub>1.8</sub>S. To further study this process, we turned to *in situ* thermal-annealing TEM so that we could directly monitor, at the single particle level, the temperature-dependent evolution of the patchy ZnS–Cu<sub>1.8</sub>S nanoparticles. *In situ* thermal TEM is a powerful technique for visualizing and identifying nanostructural changes during the heating process. <sup>38,39,44,45</sup> *In situ* TEM has previously been used to demonstrate that thermally driven solid state cation exchange of cadmium selenide to copper sulfide can be achieved and is influenced by the aggregation state of the nanoparticles. <sup>44</sup> In another study, high resolution TEM was used to visualize the dynamic structural transformation of copper sulfide through a phase transition when heated under the electron beam, allowing for the visualization of phase nucleation and propagation. <sup>46</sup>

Before beginning our *in situ* thermal TEM study, we verified that the particles were stable during long exposure times, because extended electron irradiation during *in situ* TEM analysis is known to cause sample damage and carbon contamination.<sup>47</sup> We saw no evidence of degradation, morphology change, or coalescence of particles. Beam showering before analysis was used to

minimize carbon contamination, although significant carbon deposition still occurred when exposure times exceeded five minutes. Knowing this, box furnace annealing was used in advance to identify the optimal temperature at which the ZnS domains of the patchy ZnS–Cu<sub>1.8</sub>S nanorods migrate in less than five minutes.

We loaded a sample of patchy ZnS–Cu<sub>1.8</sub>S nanorods for *in situ* thermal TEM by drop casting a dilute solution of the nanorods dispersed in hexanes onto a Protochips Fusion Select heating chip. We focused on one group of patchy particles and collected a continuous series of HAADF-STEM images as the temperature was raised stepwise from 25 °C to 50 °C and then in 50 degree increments to 100 °C, 150 °C, 200 °C, and 250 °C, pausing at each temperature to adjust the viewing window to account for drift caused by thermal expansion (Supplementary Video 1). Figure 6a shows still-frame snapshots from the video of the patchy ZnS–Cu<sub>1.8</sub>S nanorods heated to the temperatures indicated.

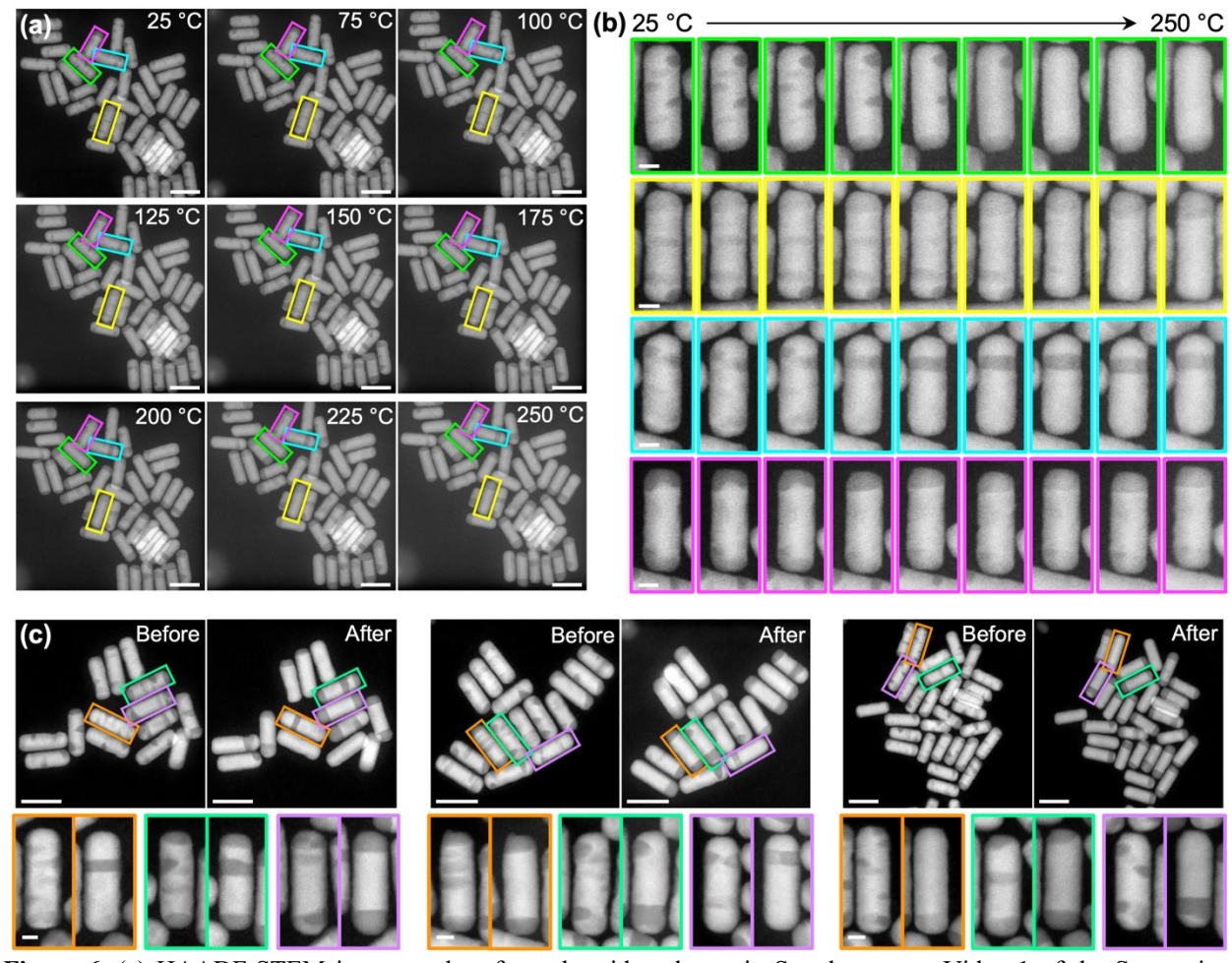


**Figure 6.** (a) HAADF-STEM images, taken from the video shown in Supplementary Video 1 of the Supporting Information, showing the evolution of the patchy rods heated *in situ* up to 250 °C. The colored boxes mark the same nanorods across the image series and cropped and enlarged images of those nanorods are shown in (b). (c) HAADF-STEM images of other groups of particles taken at room temperature before and after *in situ* heating. The colored boxes mark the same cropped nanorods before and after *in situ* heating. Scale bars of the full images are 50 nm and scale bars of cropped nanorods are 10 nm.

At 25 °C, the patchy particles have a variety of ZnS patch sizes and relative contrasts by TEM, with the darker contrast patches penetrating farther into the rod than the lighter contrast patches. Figure 6b shows four cropped nanorods throughout the heating series. The first nanorod (green) was chosen because it has many different patches with varying levels of contrast. The second nanorod (yellow) appears to have a thin central band with light contrast. This band is likely to be a patch in the top-down position that does not fully penetrate the particle, based on its location and contrast. The third nanorod (blue) has two ZnS patches sitting on either side of the nanorod in close proximity to each other. The fourth nanorod (pink) has ZnS regions at the tips of the nanorods; both of these regions are not perfectly perpendicular to the nanorod length, indicating that the ZnS region does not interface directly with the close packed plane of Cu<sub>1.8</sub>S, but rather at various angles.

Increasing the temperature to 75 °C and then to 100 °C causes only minor changes in the contrast of the ZnS domains, but overall the patchy nanorods remain largely the same as they were at 25 °C. Upon further heating to 125 °C, which goes well beyond the superionic transition temperature, more noticeable changes occur. The smallest, lighter-contrast ZnS patches that were present in the original sample visually appear to become even lighter in contrast and begin to match the contrast of the Cu<sub>1.8</sub>S region. The boundaries that separate the darker ZnS patches begin to appear more diffuse and get smaller, eventually disappearing as the temperature reaches 150 °C and beyond. While most of the patches along the body of the nanorods lighten in contrast and eventually disappear, some of the ZnS domains, particularly those located at the tips of the nanorods, become darker in contrast and grow in size.

Some of the as-synthesized patchy particles at 25 °C in Figure 6a appear to have thin central bands. Closer inspection indicates that these thin central bands are adjacent ZnS patches on opposite sides of the nanorod, a patch in a top-down orientation, or a lighter contrast band of ZnS that stretches across the nanorod without fully penetrating it. Upon thermal annealing, these regions expand, much like the regions at the tips of the nanorods. The data in Figure 6a therefore suggest that the larger ZnS patches, at either the tips or as bands located centrally in the nanorods, grow larger at the expense of the smaller ZnS patches, which disappear. This behavior is reminiscent of Ostwald ripening, which is observed in the growth of nanoparticles. 48,49 During an Ostwald ripening process that is thermodynamically favorable, larger particles are more energetically favorable than smaller ones because they have a lower surface to volume ratio and therefore a lower surface energy. 50,51 As a result, large particles grow at the expense of smaller particles, which dissolve. Here, trends in interfacial energies likely contribute similarly. The larger ZnS domains at the nanorod tips or as central bands have a lower interface to volume ratio than the smaller patches. The smaller patches, which have a higher interface to volume ratio, also have angled interfaces that exhibit poorer lattice matching than the flat interfaces that are characteristic of the nanorod tips and central bands, as discussed in Figure 2. As temperature increases, the larger ZnS domains, which have lower interfacial energies, grow at the expense of the smaller domains, which have higher interfacial energies and therefore disappear. To achieve such a process, the Zn<sup>2+</sup> from the smaller ZnS domains can diffuse rapidly through the Cu<sub>1.8</sub>S, which is in its superionic state at the temperatures (>100 °C) where such behavior is observed, to access the preferred larger ZnS domains. There is no chemical pathway for dissolution to occur, and ZnS and Cu<sub>1.8</sub>S remain overall immiscible and phase segregated. As a result, thermally induced material transfer lowers the energy of the system by restructuring the composition distribution in the heterostructured nanorods.

In addition to the still-frame images in Figure 6a, which were taken from videos during *in situ* heating in the TEM, Figure 6c shows HAADF-STEM images of several collections of patchy ZnS—Cu<sub>1.8</sub>S nanorods taken before and after heating to 250 °C in the TEM. Also, in addition to providing further insights into how the patchy ZnS—Cu<sub>1.8</sub>S nanorods thermally transform, the images in Figure 6c also confirm that the thermally-transformed nanorods are recoverable to room temperature and therefore stable. In other words, they do not revert back to the as-synthesized patchy particles upon cooling back to room temperature after heating, but instead retain the features that emerged upon heating.

To further build on the observations in Figure 6, which identified thermal transformations for a variety of patchy ZnS–Cu<sub>1.8</sub>S nanorods, we synthesized simplified single-patch and double-patch nanorods by modifying the heating protocols, as shown in Figure 1. The single-patch particles had, as the majority product, a central ZnS patch along the length of the nanorod, along with a minor subpopulation of single tipped rods. The double-patch particles have two central ZnS patches along the length of the rod, a ZnS domain at both tips, or one central ZnS patch as well as one ZnS tip. The single- and double-patch samples were combined, and this mixture (as a new set of experiments, shown in Figure 7) was subjected to the same *in situ* TEM heating profile as the patchy ZnS–Cu<sub>1.8</sub>S nanorods shown in Figure 6. By comparing the images from before and after heating to 250 °C (Figure 7), we can analyze the thermal evolution of the ZnS domains more quantitatively than in Figure 6 because of the simplified system containing only single- and double-patch (instead of multi-patch) nanorods.

Across ten images, one of which is shown in Figure 7 and all of which are shown in Figure S4, 353 nanorods were analyzed. We categorized the nanorods based on the number and placement of the ZnS domains. All as-synthesized nanorods could be assigned to five categories and included 21 with a single tip of ZnS, 34 with a central patch of ZnS, 143 with ZnS at both tips, 140 with a central patch and one tip of ZnS, and 15 with two central patches of ZnS. After annealing up to 250 °C in situ in the TEM, 63% of the nanorods having ZnS at both tips transformed into singletip ZnS–Cu<sub>1.8</sub>S nanorods, where the ZnS at the one tip migrated to combine with the other ZnS tip. In many cases, the smaller ZnS tip migrated to the larger ZnS tip. The remaining double tipped rods were unchanged, potentially because the ZnS domains already sit at the favored tips of the nanorod. Of the nanorods containing one central patch and one single tip of ZnS, 79% converged to one domain of ZnS, with a majority (66%) of the particles experiencing migration, where the central patch migrated to, and combined with, the single ZnS domain at the tip. This behavior is likely due to the tip being the preferential location for the ZnS domain. At the tip, there is only one interface between the ZnS and the Cu<sub>1.8</sub>S, whereas forming a central band or a patch results in at least two interfaces. For the double-patch nanorods with two central patches, all of them converged to nanorods having one larger central patch or band, with one ZnS patch remaining in place while the other migrated and combined with it. The migration of one central domain to another removes one set of unfavorable interfaces. However, it is interesting that there is no formation of a new domain at the tip. These nanorods are unique in that there is not an existing domain already at the tip. Upon migration, we did not observe the disappearance of both ZnS patches to form a patch at a different location such as the more favorable tip. This observation tells us that a new domain will not form, and the energy required to nucleate a new domain of ZnS at the tip is too high for this system.

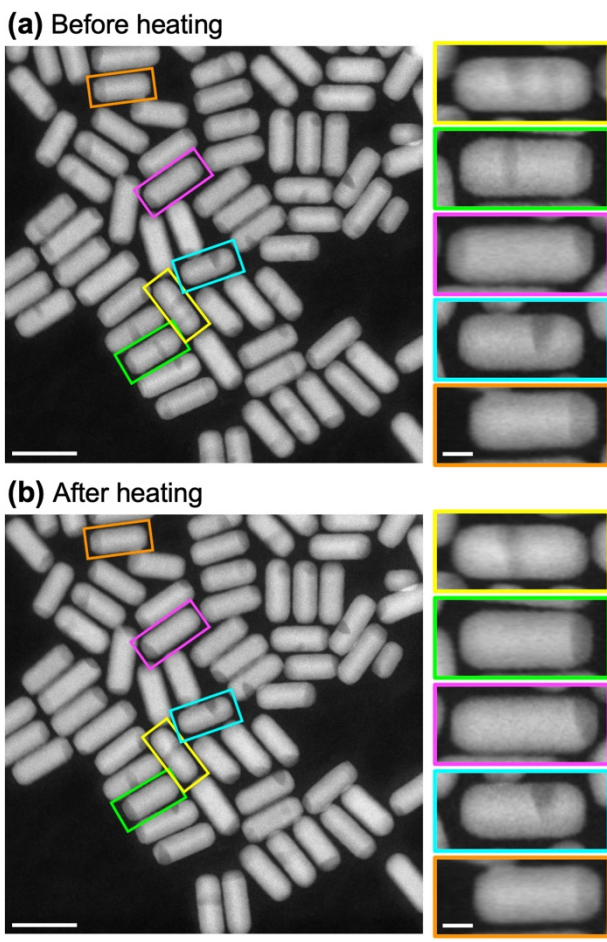


**Figure 7.** HAADF-STEM images of various ZnS–Cu<sub>1.8</sub>S nanorod heterostructures (a) before and (b) after *in situ* heating to 250 °C. Cropped images show examples of particles with ZnS domains in different positions on the rod (from top to bottom): two central patches, one central patch and one tip, double tips, one central patch, and a single tip. The colored boxes mark the same nanorods across the image series. Scale bars in full images are 50 nm and scale bars for cropped nanorods are 10 nm.

The statistics of patch migration across all of the double-patch nanorods trend with the predicted interfacial energies. From the perspective of interfaces between the ZnS and Cu<sub>1.8</sub>S regions in the double-patch nanorods, the single-tipped nanorods would be expected to be most stable because they minimize the number of interfaces and maximize interfaces that have the best lattice matching. Based on the number of interfaces and lattice matching, the nanorods having one ZnS tip along with one central ZnS patch would be next in stability, with double-patch nanorods being the least favorable because of their high interfacial area and components of interfaces that are not along the most lattice-matched planes. The observation that thermal migration tended toward the higher-stability configurations reinforces the energetic driving force toward transformation from a higher-energy as-synthesized form to a lower-energy, more stable form. This analysis further suggests that the patches may be a kinetically-trapped state that requires heating to transform to the more commonly observed ZnS–Cu<sub>1.8</sub>S nanorods, which have ZnS domains on one or both tips or as a flat central band.

We also analyzed the thermal evolution of the nanorods containing a single domain of ZnS. For these systems, the role of interfaces can be more explicitly elucidated, as there is only one ZnS

domain, and therefore no ability for migration to occur from one ZnS domain to another. Of all the synthetically-accessible ZnS–Cu<sub>1.8</sub>S nanorods, the most stable is one that contains only a single domain of ZnS at the tip because it includes a single interface along a low-strain close packed plane. The single-patch nanorods are particularly interesting to consider. While there is still only one ZnS domain, the interfaces and area between the ZnS and Cu<sub>1.8</sub>S domains are different than those in the central-band, single-tip, and double-tip nanorods. We hypothesized that if these different interfaces played a large role in ZnS migration in the patchy particles, the central-patch ZnS domain would prefer to migrate to the tip, forming the most stable type of heterostructured nanorod. Unexpectedly, we observed that none of the single patch nanorods changed during annealing and single ZnS patches near the center of a nanorod remained stationary. These results suggest that Ostwald ripening plays the largest role in driving the movement of the ZnS domains in the multi-patch particles, and while the type of interfaces between the ZnS and Cu<sub>1.8</sub>S regions can play a role in determining the likelihood of a patch migrating, it is not the primary driver.

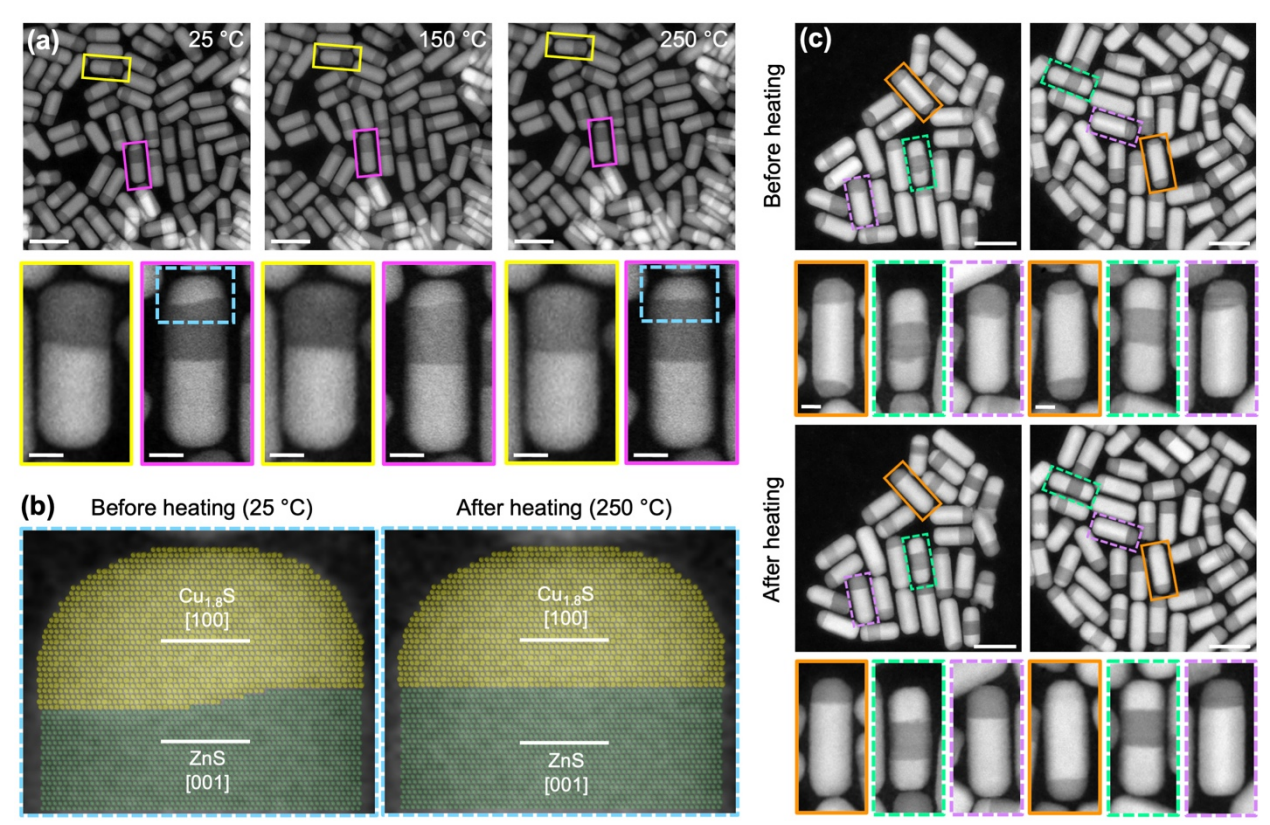


**Figure 8.** (a) HAADF-STEM images, taken from the video shown in Supplementary Video 2 of the Supporting Information, showing the evolution of the mixed population of double tipped, single tipped, and central band particles before and after heating *in situ* to 250 °C using the same heating profile as was used with the patchy rods. The colored boxes mark the same cropped nanorods across the image series. The dashed light blue box highlights the change in the interface before and after heating. (b) A false-colored crystal structure of roxbyite (yellow) and wurtzite ZnS (green) is overlayed on an enlarged image of the interface highlighted in the dashed light blue box in (a), showing the subtle change during heating. (c) HAADF-STEM images of other groups of nanorods taken at room temperature before and after *in situ* heating. Nanorods outlined with a solid box correspond to examples where the smaller domain in the double tipped nanorods migrates to combine with the larger domain. The nanorods outlined with a dashed box correspond to examples where the ZnS/Cu<sub>1.8</sub>S interface aligns parallel to the close packed (100) planes after heating. Scale bars of the full images are 50 nm and scale bars of cropped nanorods are 10 nm.

Figure 8a shows HAADF-STEM still-frame images from a video (Supplementary Video 2) taken during in situ heating of a different sample of heterostructured ZnS-Cu<sub>1.8</sub>S nanorods that begin with largely the preferred interfaces having the closest lattice matching, along with no patches. The mixed-population sample shown in Figure 1, and discussed earlier, contains single-tip ZnS-Cu<sub>1.8</sub>S, central band Cu<sub>1.8</sub>S–ZnS–Cu<sub>1.8</sub>S, and double–tip ZnS–Cu<sub>1.8</sub>S–ZnS heterostructured nanorods. This sample was subjected to the same in situ thermal TEM heating profile as the patchy ZnS-Cu<sub>1.8</sub>S nanorods. As discussed earlier, the most closely matched lattice spacings of ZnS and Cu<sub>1.8</sub>S are in the stacking direction of the close-packed planes, which include ZnS (001) and Cu<sub>1.8</sub>S (100), and are perfectly perpendicular to the nanorod length. Unsurprisingly, the interfaces between ZnS and Cu<sub>1.8</sub>S in the as-synthesized ZnS-Cu<sub>1.8</sub>S nanorods are rarely perfect. These interfaces may appear flat (i.e., perpendicular to the length of the nanorod) at low magnification, but at higher magnification they often adopt various angles due to step edges, stacking faults, and jagged boundaries. The data in Figure 8a confirm that many of the as-synthesized ZnS-Cu<sub>1.8</sub>S nanorods have angled interfaces; data at all temperatures are shown in Figure S5. Upon heating to 150 °C and then 250 °C, the interfaces between ZnS and Cu<sub>1.8</sub>S that are angled gradually appear to become flatter so that they are aligned to a greater extent along their ZnS(001)/Cu<sub>1.8</sub>S(100) interface. This can be seen clearly in the single tip cropped particle. At 25 °C, the ZnS/Cu<sub>1.8</sub>S interface slants down from left to right, while after annealing the interface is perpendicular to the length of the nanorod. Figure 8b shows an enlarged region of the Cu<sub>1.8</sub>S/ZnS interface on the central band particle (dashed blue box) with a false-colored crystal structure overlayed to illustrate the subtle change in the interface after heating.

Figure 8c shows HAADF-STEM images of several collections of the mixed-population sample containing single—tip ZnS—Cu<sub>1.8</sub>S, central band Cu<sub>1.8</sub>S—ZnS—Cu<sub>1.8</sub>S, and double—tip ZnS—Cu<sub>1.8</sub>S—ZnS heterostructured nanorods taken before and after heating to 250 °C in the TEM. A cropped particle for each of the three types of nanorods is shown before and after heating. As described above, the interfaces in the single—tip ZnS—Cu<sub>1.8</sub>S and central band Cu<sub>1.8</sub>S—ZnS—Cu<sub>1.8</sub>S nanorods flatten to align the ZnS(001)/Cu<sub>1.8</sub>S(100) interface. However, for some of the double tip rods, it is evident that a smaller ZnS region at the tips of a nanorod can migrate to combine with a ZnS region at the other tip through a process that requires the Zn<sup>2+</sup> ions from the smaller region to diffuse nearly 50 nm through the rod. This observation lends further support to the idea that Ostwald ripening is governing the temperature-dependent migration of the ZnS domains in the patchy ZnS—Cu<sub>1.8</sub>S nanorods and that the temperature being above the superionic transition of Cu<sub>1.8</sub>S facilitates the fast and long-distance diffusion.

## **CONCLUSIONS**

Here, we synthesized a library of different types of patchy ZnS–Cu<sub>1.8</sub>S nanorods through cation exchange of Zn<sup>2+</sup> with Cu<sub>1.8</sub>S, as well as simplified single and double patch particles. Upon annealing in solution, in a furnace, and *in situ* in a TEM, the ZnS patches migrate via Zn<sup>2+</sup> diffusion through the nanorods to form fewer, larger ZnS domains. This temperature-dependent dynamic behavior is likely enabled by the superionic nature of copper sulfide above ~100 °C. Above this temperature, the copper sulfide can be thought of as having a highly mobile sea of cations surrounding a rigid sulfur anion lattice, whereby the Zn<sup>2+</sup> can easily migrate from small ZnS domains to larger domains through a process that is reminiscent of Ostwald ripening. Statistical analysis shows that ZnS domain migration favors the tips and complete central bands, which are

the most common intraparticle frameworks that are observed through direct cation exchange because the resulting interfaces between ZnS and Cu<sub>1.8</sub>S are those that align the close-packed planes in a way that minimizes lattice strain. The observed dynamic behavior of the ZnS patches at high temperatures provides possible insights into how partial cation exchange processes occur and evolve. The data suggest that at early time points during partial cation exchange, patches of ZnS in Cu<sub>1.8</sub>S originally form as kinetically trapped domains, and further heating helps revert them to the commonly observed products, which have full ZnS bands at the tips or in the middle, that ultimately minimize the energy of the system. These insights provide a glimpse of the potential temperature-dependent dynamic nature of the domains incorporated within heterostructured nanoparticles and also provide mechanistic insights for designing and synthesizing energy-minimized products having targeted architectures and compositional arrangements.

## **EXPERIMENTAL SECTION**

## Chemicals

1-dodecanethiol (1-DDT, Sigma Aldrich,  $\geq$ 98%), *tert*-dodecanethiol (t-DDT, Sigma-Aldrich, mixture of isomers,  $\geq$ 98.5%), isopropyl alcohol (IPA, Millipore), ethanol (Koptec), toluene (Millipore), hexanes (Millipore), octadecene (ODE, Sigma-Aldrich, 90%), oleylamine (OLAM, Sigma-Aldrich, 70%), benzyl ether (BE, ThermoScientific, 99%), trioctylphosphine oxide (TOPO, Sigma-Aldrich, 98%), trioctylphosphine (TOP, Sigma-Aldrich,  $\geq$ 99%), copper (II) nitrate trihydrate (Cu(NO<sub>3</sub>)<sub>2</sub>·3H<sub>2</sub>O, Sigma-Aldrich,  $\geq$ 99%), and zinc chloride (ZnCl<sub>2</sub>, anhydrous, Sigma-Aldrich, 97%). All chemicals were used as received.

# Synthesis of roxbyite (Cu<sub>1.8</sub>S) nanorods

Copper sulfide nanorods were synthesized by adding 843 mg of  $Cu(NO_3)_2 \cdot 3H_2O$ , 8.7 g of TOPO, 45 mL of ODE, and 750  $\mu$ L of OLAM to a 3-neck round bottom flask. The solution was placed under vacuum and heated to 80 °C for 30 minutes. The flask was put under a flow of Ar and a 22.5 mL mixture of 10:1 t-DDT:1-DDT was rapidly injected. The temperature was raised to 180 °C within 5 minutes. The solution stirred for 20 minutes and was removed from heat to be cooled by a water bath. The nanorods were precipitated by a 1:1 mixture of IPA:acetone and washed by centrifugation and resuspension in toluene four times. <sup>11</sup>

## Preparation of cation exchange solutions

Cation exchange solutions of 0.073 mmol/mL Zn<sup>2+</sup> and 0.018 mmol/mL Cd<sup>2+</sup> were prepared by adding the desired salt (250 mg ZnCl<sub>2</sub> or 84.1 mg CdCl<sub>2</sub>) to a round bottom flask with 15 mL of BE, 8 mL of OLAM, and 2 mL of ODE. The solution was placed under vacuum and heated to 100 °C for 1 hour. The flask was placed under a blanket of Ar and heated up to 200 °C for 30 minutes before cooling to room temperature. The solutions were stored in septum capped vials.<sup>10</sup>

## Synthesis of patchy ZnS–Cu<sub>1.8</sub>S nanorods

Patchy ZnS–Cu<sub>1.8</sub>S nanorods were prepared by placing a 50 mL, 3-neck round bottom flask with 1.89 mL Zn<sup>2+</sup> exchange solution, 15 mL of BE, 4 mL of OLAM, and 2 mL of ODE under vacuum and heating to 100 °C for 30 minutes. The solution was placed under a blanket of Ar and cooled to 50 °C. In a septum capped vial, 20 mg of Cu<sub>1.8</sub>S nanorods were dried and flushed with Ar before 3 mL of TOP were added. The vial was sonicated for 45 minutes and the nanorod solution was

injected into the flask before cycling with Ar three times. The reaction was stirred (45 minutes for small patches or 1.5 hours for large patches) and removed from heat to cool in an ice bath. The product was precipitated in a 1:1 mixture of IPA:acetone and washed by centrifugation and resuspension in toluene 5-7 times. The nanorods were drop cast on TEM grids immediately for analysis.

## Synthesis of patchy ZnS–CdS nanorods

Patchy ZnS–CdS nanorods were prepared by placing a 50 mL, 3-neck round bottom flask with 3.66 mL Cd<sup>2+</sup> exchange solution, 7.5 mL of BE, 2 mL of OLAM, and 1 mL of ODE under vacuum and heating to 100 °C for 30 minutes. The solution was placed under a blanket of Ar and cooled to 70 °C. Separately, 10 mg of patchy ZnS–Cu<sub>1.8</sub>S nanorods were dried and flushed with Ar before 1.5 mL of TOP was added and sonicated for 45 minutes. The nanorod solution was injected into the flask before cycling with Ar three times. The reaction was stirred for 1 hour and removed from heat to cool in an ice bath. The product was precipitated in a 1:1 mixture of IPA:acetone and washed by centrifugation and resuspension in toluene four times.

## Synthesis of a mixture of single tip, central band, and double tip ZnS/Cu<sub>1.8</sub>S nanorods

A sample consisting of a mixture of the cation exchange products ZnS–Cu<sub>1.8</sub>S, Cu<sub>1.8</sub>S–ZnS–Cu<sub>1.8</sub>S, and ZnS–Cu<sub>1.8</sub>S–ZnS was obtained by adding 0.314 mL Zn<sup>2+</sup> exchange solution, 15 mL of BE, 4 mL of OLAM, and 2 mL of ODE to a 50 mL, 3-neck round bottom flask. The flask was placed under vacuum and heated to 100 °C for 30 minutes. The solution was placed under a blanket of Ar and cooled to 50 °C. In a septum capped vial, 20 mg of Cu<sub>1.8</sub>S nanorods were dried and flushed with Ar before 3 mL of TOP were added. The vial was sonicated for 45 minutes and the nanorod solution was injected into the flask before cycling with Ar three times. The reaction stirred at 50 °C for 1 hour before the temperature was raised to 160 °C and then was stirred for another 30 minutes. The nanorods were precipitated in IPA and washed by centrifugation and resuspension in toluene four times.

## Synthesis of single tip ZnS–Cu<sub>1.8</sub>S nanorods

Single tip nanorods were obtained by adding 0.314~mL Zn<sup>2+</sup> exchange solution, 15 mL of BE, 4 mL of OLAM, and 2 mL of ODE to a 50 mL, 3-neck round bottom flask. The flask was placed under vacuum and heated to 100~°C for 30 minutes. The solution was placed under a blanket of Ar and heated to 120~°C. In a septum capped vial, 20 mg of Cu<sub>1.8</sub>S nanorods (1 equivalent) were dried and flushed with Ar before 3 mL of TOP were added. The vial was sonicated for 45 minutes and the nanorod solution was injected into the flask before cycling with Ar three times. The reaction stirred for 30 minutes and was removed from heat to cool in an ice bath. The nanorods were precipitated in IPA and washed by centrifugation and resuspension in toluene four times.  $^{10}$ 

## Synthesis of central band Cu<sub>1.8</sub>S–ZnS–Cu<sub>1.8</sub>S nanorods

Central band nanorods were obtained by adding 0.314 mL Zn<sup>2+</sup> exchange solution, 15 mL of BE, 4 mL of OLAM, and 2 mL of ODE to a 50 mL, 3-neck round bottom flask. The flask was placed under vacuum and heated to 100 °C for 30 minutes. The solution was placed under a blanket of Ar and cooled to room temperature. In a septum capped vial, 20 mg of Cu<sub>1.8</sub>S nanorods (1 equivalent) were dried and flushed with Ar before 3 mL of TOP were added. The vial was sonicated for 45 minutes, and the nanorod solution was injected into the flask before cycling with Ar three times. Right after injection, the temperature ramped up to 100 °C at a rate of 10 °C/min and stirred for

30 minutes. The flask was removed from heat to cool in an ice bath. The nanorods were precipitated in IPA and washed by centrifugation and resuspension in toluene four times.<sup>10</sup>

# Synthesis of single patch ZnS-Cu<sub>1.8</sub>S nanorods

Single patch nanorods were obtained modifying the central band  $Cu_{1.8}S$ –ZnS– $Cu_{1.8}S$  nanorod procedure. A solution of 0.189 mL  $Zn^{2+}$  exchange solution, 15 mL of BE, 4 mL of OLAM, and 2 mL of ODE was added to a 50 mL, 3-neck round bottom flask. The flask was placed under vacuum and heated to 100 °C for 30 minutes. The solution was placed under a blanket of Ar and cooled to room temperature. In a septum capped vial, 20 mg of  $Cu_{1.8}S$  nanorods were dried and flushed with Ar before 3 mL of TOP were added. The vial was sonicated for 45 minutes and the nanorod solution was injected into the flask before cycling with Ar three times. Right after injection, the temperature ramped up to 90 °C at a rate of 10 °C/min and was immediately cooled in an ice bath. The nanorods were precipitated in IPA and washed by centrifugation and resuspension in toluene four times.

## Synthesis of double patch ZnS–Cu<sub>1.8</sub>S nanorods

Double patch nanorods were obtained by modifying the patchy ZnS–Cu<sub>1.8</sub>S nanorod procedure. A solution of 0.189 mL Zn<sup>2+</sup> exchange solution, 15 mL of BE, 4 mL of OLAM, and 2 mL of ODE was added to a 50 mL, 3-neck round bottom flask. The flask was placed under vacuum and heated to  $100\,^{\circ}$ C for 30 minutes. The solution was placed under a blanket of Ar and cooled to  $50\,^{\circ}$ C. In a septum capped vial, 20 mg of Cu<sub>1.8</sub>S nanorods were dried and flushed with Ar before 3 mL of TOP were added. The vial was sonicated for 45 minutes and the nanorod solution was injected into the flask before cycling with Ar three times. Right after injection, the temperature ramped up to  $80\,^{\circ}$ C at a rate of  $10\,^{\circ}$ C/min and stirred for 3 minutes. The flask was removed from heat to cool in an ice bath. The nanorods were precipitated in IPA and washed by centrifugation and resuspension in toluene four times.

## *In situ* TEM annealing

A micropipette was used to drop cast 8  $\mu$ L of a dilute suspension of nanoparticles in hexanes on a carbon coated Fusion Select heating chip. *In situ* experiments were completed using the Protochips Aduro heating system consisting of a TEM holder, power supply, and control software. Images were acquired using he Velox software in continuous mode with a dwell time of 1  $\mu$ s, a frame time of 1.3 seconds, and a temperature ramp rate of 100 °C/min.

## Box furnace annealing

Solid state annealing was done in a box furnace fitted with an external temperature probe using a Si plate as an annealing substrate. The nanoparticles were concentrated and drop cast in toluene on a zero background Si plate. After the solvent evaporated, the plate was quickly placed in the box furnace at the desired temperature for the desired time. The plate was then removed, and the particles could be directly analyzed by XRD or recovered in a powder by gently scraping them off the plate. To visualize the exact same particles before and after annealing, carbon coated, 400-mesh Au London finder grids from Electron Microscopy Sciences were used as an annealing substrate. A dilute suspension of nanoparticles in hexanes were drop cast on the finder grids and analyzed by TEM. The finder grid was then placed on top of a Si wafer in the box furnace for annealing and was re-analyzed by TEM after being removed.

## Solution annealing

A solution of 7.5 mL ODE and 1 mL OLAM were added to a 25 mL, 3-neck round bottom flask. The flask was placed under vacuum and heated to  $100\,^{\circ}\text{C}$  for 30 minutes. The solution was placed under a blanket of Ar and heated to the desired temperature for annealing ( $50-160\,^{\circ}\text{C}$ ). In a septum capped vial, 20 mg of Cu<sub>1.8</sub>S nanorods were dried and flushed with Ar before 1.5 mL of ODE were added. The vial was sonicated for 15 minutes before the particle solution was injected into the flask and cycled with Ar three times. The reaction stirred for the desired amount of time (5 minutes to 5 hours).

## Characterization

Powder X–ray diffraction (XRD) data was collected on an Empyrean diffractometer using Cu Kα radiation. Nanoparticle samples were deposited onto a zero background Si sample holder. Crystal structures were simulated using CrystalMaker and reference patterns were generated using CrystalDiffract, distributed by CrystalMaker Software Ltd, Oxford, England (www.crystalmaker.com). High–angle annular dark field (HAADF) and scanning transmission electron microscopy energy dispersion spectroscopy (STEM–EDS) images were collected using a Ceta camera and a SuperX EDS detector using the Bruker Esprit software on a FEI Talos F200X S/TEM at an accelerating voltage of 200 kV.

## Differential scanning calorimetry

Differential scanning calorimetry (DSC) data were collected on a TA Instruments DSC Q2000 V24.11 using a Standard Cell FC under nitrogen atmosphere. For each sample, the heating/cooling rate was 10 °C/minute from 20 °C to 250 °C and was cycled four times. DSC data was analyzed using TA Universal Analysis. For analysis by differential scanning calorimetry, the as-synthesized Cu<sub>1.8</sub>S nanorods were further subjected to cation exchange conditions without the presence of an exchange cation. To a 50 mL, 3-neck round bottom flask with 15 mL of BE, 4 mL of OLAM, and 2 mL of ODE were placed under vacuum and heated to 100 °C for 30 minutes. The solution was placed under a blanket of Ar and cooled to 50 °C. In a septum capped vial, 20 mg of Cu<sub>1.8</sub>S nanorods were dried and flushed with Ar before 3 mL of TOP were added. The vial was sonicated for 45 minutes and the nanorod solution was injected into the flask before cycling with Ar three times. The solution stirred for 30 minutes and removed from heat to cool in an ice bath. The product was precipitated in a 1:1 mixture of IPA:acetone and washed by centrifugation and resuspension in toluene four times. ZnS nanorods for DSC analysis were prepared by placing a 50 mL, 3-neck round bottom flask with 1.89 mL Zn<sup>2+</sup> exchange solution, 15 mL of BE, 4 mL of OLAM, and 2 mL of ODE under vacuum and heating to 100 °C for 30 minutes. The solution was placed under a blanket of Ar and heated to 120 °C. In a septum capped vial, 20 mg of Cu<sub>1.8</sub>S nanorods were dried and flushed with Ar before 3 mL of TOP were added. The vial was sonicated for 45 minutes and the nanorod solution was injected into the flask before cycling with Ar three times. The reaction was stirred for 30 minutes and removed from heat to cool in an ice bath. The product was precipitated in a 1:1 mixture of IPA:acetone and washed by centrifugation and resuspension in toluene four times.<sup>11</sup>

#### ASSOCIATED CONTENT

#### **Supporting Information**

The Supporting Information is available free of charge on the ACS Publications website.

- Additional TEM, STEM-EDS, and DSC data (PDF).
- Supplementary videos (MP4)

### **AUTHOR INFORMATION**

## **Corresponding Author**

**Raymond E. Schaak** – Department of Chemistry, Department of Chemical Engineering, and Materials Research Institute, The Pennsylvania State University, University Park, Pennsylvania 16802, United States; Email: res20@psu.edu

## **Authors**

**Haley L. Young** – Department of Chemistry, The Pennsylvania State University, University Park, Pennsylvania 16802, United States

Enrique D. Gomez – Department of Chemical Engineering, Department of Materials Science and Engineering, and Materials Research Institute, The Pennsylvania State University, University Park, Pennsylvania 16802, United States

#### **Notes**

The authors declare no competing financial interest.

## **ACKNOWLEDGMENT**

This work was supported by the U.S. National Science Foundation under grant DMR-2210442. This material is based upon work supported by the National Science Foundation Graduate Research Fellowship Program under Grant No. (DGE1255832). Any opinions, findings, and conclusions or recommendations expressed in this material are those of the author(s) and do not necessarily reflect the views of the National Science Foundation. TEM, XRD, and DSC data were acquired at the Materials Characterization Lab of the Penn State Materials Research Institute. The authors thank Jennifer Gray for *in situ* TEM support.

#### **REFERENCES**

- (1) Schaak, R. E.; Steimle, B. C.; Fenton, J. L. Made-to-Order Heterostructured Nanoparticle Libraries. *Acc. Chem. Res.* **2020**, *53*, 2558–2568. DOI: 10.1021/acs.accounts.0c00520
- (2) Ha, M.; Kim, J. H.; You, M.; Li, Q.; Fan, C.; Nam, J. M. Multicomponent Plasmonic Nanoparticles: From Heterostructured Nanoparticles to Colloidal Composite Nanostructures. *Chem. Rev.* **2019**, *119*, 12208–12278. DOI: 10.1021/acs.chemrev.9b00234
- (3) Oh, N.; Kim, B. H.; Cho, S. Y.; Nam, S.; Rogers, S. P.; Jiang, Y.; Flanagan, J. C.; Zhai, Y.; Kim, J. H.; Lee, J.; Yu, Y.; Cho, Y. K.; Hur, G.; Zhang, J.; Trefonas, P.; Rogers, J. A.; Shim, M. Double-Heterojunction Nanorod Light-Responsive LEDs for Display Applications. *Science* **2017**, *355*, 616–619. DOI: 10.1126/science.aal2038
- (4) Shan, B.; Wang, H.; Li, L.; Zhou, G.; Wen, Y.; Chen, M.; Li, M. Rationally designed dual-plasmonic gold nanorod@cuprous selenide hybrid heterostructures by regioselective overgrowth for *in vivo* photothermal tumor ablation in the second near-infrared biowindow. *Theranostics* **2020**, *10*, 11656–11672. DOI: 10.7150/thno.51287
- (5) Drake, G. A.; Keating, L. P.; Shim, M. Design Principles of Colloidal Nanorod Heterostructures. *Chem. Rev.* **2023**, *123*, 3761–3789. DOI: 10.1021/acs.chemrev.2c00410
- (6) Li, H.; Zanella, M.; Genovese, A.; Povia, M.; Falqui, A.; Giannini, C.; Manna, L. Sequential Cation Exchange in Nanocrystals: Preservation of Crystal Phase and Formation of Metastable Phases. *Nano Lett.* **2011**, *11*, 4964–4970. DOI: 10.1021/nl202927a
- (7) Ha, D. H.; Caldwell, A. H.; Ward, M. J.; Honrao, S.; Mathew, K.; Hovden, R.; Koker, M. K. A.; Muller, D. A.; Hennig, R. G.; Robinson, R. D. Solid–Solid Phase Transformations Induced through Cation Exchange and Strain in 2D Heterostructured Copper Sulfide Nanocrystals. *Nano Lett.* 2014, 14, 7090–7099. DOI: 10.1021/nl5035607
- (8) Son, D. H.; Hughes, S. M.; Yin, Y.; Alivisatos, A. P. Cation Exchange Reactions in Ionic Nanocrystals. *Science* **2004**, *306*, 1009–1012. DOI: 10.1126/science.1103755
- (9) Robinson, R. D.; Sadtler, B.; Demchenko, D. O.; Erdonmez, C. K.; Wang, L. W.; Alivisatos, A. P. Spontaneous Superlattice Formation in Nanorods Through Partial Cation Exchange. *Science* 2007, 317, 355–358. DOI: 10.1126/science.1142593
- (10) Steimle, B. C.; Fenton, J. L.; Schaak, R. E. Rational construction of a scalable heterostructured nanorod megalibrary. **2020**, *367*, 418–424. DOI: 10.1126/science.aaz1172
- (11) Fenton, J. L.; Steimle, B. C. Tunable intraparticle frameworks for creating complex heterostructured nanoparticle libraries. **2018**, *517*, 513–517. DOI: 10.1126/aar5597
- (12) Li, P.; Wei, Z.; Wu, T.; Peng, Q.; Li, Y. Au–ZnO Hybrid Nanopyramids and Their Photocatalytic Properties. *J. Am. Chem. Soc.* **2011**, *133*, 5660–5663. DOI: 10.1021/ja111102u
- (13) Shaviv, E.; Schubert, O.; Alves-Santos, M.; Goldoni, G.; Di Felice, R.; Vallée, F.; Del Fatti, N.; Banin, U.; Sönnichsen, C. Absorption Properties of Metal–Semiconductor Hybrid Nanoparticles. *ACS Nano* **2011**, *5*, 4712–4719. DOI: 10.1021/nn200645h
- (14) Chen, P. C.; Liu, X.; Hedrick, J. L.; Xie, Z.; Wang, S.; Lin, Q. Y.; Hersam, M. C.; Dravid, V. P.; Mirkin, C. A. Polyelemental nanoparticle libraries. *Science* **2016**, *352*, 1565–1569. DOI: 10.1126/science.aaf8402
- (15) Zhang, Y.; Chen, Z.; Cao, D.; Zhang, J.; Zhang, P.; Tao, Q.; Yang, X. Concurrence of spinodal decomposition and nano-phase precipitation in a multi-component AlCoCrCuFeNi high-entropy alloy. *J. Mater. Res.* **2019**, *8*, 726–736. DOI: 10.1016/j.jmrt.2018.04.020

- (16) Wang, P.; Chen, J.; Sun, B.; Zhu, D.; Cao, Y. Effects of annealing process parameters on microstructural evolution and strength-ductility combination of CoCrFeMnNi high-entropy alloy. *Mater. Sci. Eng. A* **2022**, *840*, 142880. DOI: 10.1016/j.msea.2022.142880
- (17) Steimle, B. C. Design and Synthesis of Inorganic Nanoparticle Heterostructures Using Cation Exchange Transformations. Ph.D. Thesis, The Pennsylvania State University, State College, PA, 2021.
- (18) Bueno, S. L. A.; Leonardi, A.; Kar, N.; Chatterjee, K.; Zhan, X.; Chen, C.; Wang, Z.; Engel, M.; Fung, V.; Skrabalak, S. E. Quinary, Senary, and Septenary High Entropy Alloy Nanoparticle Catalysts from Core@Shell Nanoparticles and the Significance of Intraparticle Heterogeneity. *ACS Nano* **2022**, *16*, 18873–18885. DOI: 10.1021/acsnano.2c07787
- (19) Chen, Y.; Zhan, X.; Bueno, S. L. A.; Shafei, I. H.; Ashberry, H. M.; Chatterjee, K.; Xu, L.; Tang, Y.; Skrabalak, S. E. Synthesis of monodisperse high entropy alloy nanocatalysts from core@shell nanoparticles. *Nanoscale Horiz.* **2021**, *6*, 231–237. DOI: 10.1039/d0nh00656d
- (20) Chen, P. C.; Liu, M.; Du, J. S.; Meckes, B.; Wang, S.; Lin, H.; Dravid, V. P.; Wolverton, C.; Mirkin, C. A. Interface and heterostructure design in polyelemental nanoparticles. *Science* **2019**, *363*, 959–964. DOI: 10.1126/science.aav4302
- (21) Lv, B.; Liu, Y.; Wu, W.; Xie, Y.; Zhu, J. L.; Cao, Y.; Ma, W.; Yang, N.; Chu, W.; Jia, Y.; Wei, J.; Sun, J. L. Local large temperature difference and ultra-wideband photothermoelectric response of the silver nanostructure film/carbon nanotube film heterostructure. *Nat Commun* **2022**, *13*, 1835. DOI: 10.1038/s41467-022-29455-6
- (22) Cui, X.; Ruan, Q.; Zhuo, X.; Xia, X.; Hu, J.; Fu, R.; Li, Y.; Wang, J.; Xu, H. Photothermal Nanomaterials: A Powerful Light-to-Heat Converter. *Chem. Rev.* **2023**, *123*, 6891–6952. DOI: 10.1021/acs.chemrev.3c00159
- (23) Widstrom, A. L.; Lear, B. J. Nanoscale heat for organic transformations: a photothermally driven retro Diels–Alder reaction. *Appl Nanosci* **2020**, *10*, 819–825. DOI: 10.1007/s13204-019-01175-2
- (24) Fortenbaugh, R. J.; Carrozzi, S. A.; Lear, B. J. Photothermal Control over the Mechanical and Physical Properties of Polydimethylsiloxane. *Macromolecules* **2019**, *52*, 3839–3844. DOI: 10.1021/acs.macromol.9b00134
- (25) Wei, N.; Wang, H. Q.; Zheng, J. C. Nanoparticle manipulation by thermal gradient. *Nanoscale Res Lett* **2012**, *7*, 154. DOI: 10.1186/1556-276X-7-154
- (26) Theja, V. C. S.; Karthikeyan, V.; Assi, D. S.; Roy, V. A. L. Insights into the Classification of Nanoinclusions of Composites for Thermoelectric Applications. *ACS Appl. Electron. Mater.* **2022**, *4*, 4781–4796. DOI: 10.1021/acsaelm.2c00617
- (27) Parás-Hernández, F. U.; Fabián-Mijangos, A.; Cardona-Castro, M. A.; Alvarez-Quintana, J. Enhanced performance nanostructured thermoelectric converter for self-powering health sensors. *Nano Energy* **2020**, *74*, 104854. DOI: 10.1016/j.nanoen.2020.104854
- (28) Choi, K.; Kim, D.; Chung, W.; Cho, C.; Kang, S. W. Nanostructured thermoelectric composites for efficient energy harvesting in infrastructure construction applications. *Cem. Concr. Compos.* **2022**, *128*, 104452. DOI: 10.1016/j.cemconcomp.2022.104452
- (29) Steimle, B. C.; Fagan, A. M.; Butterfield, A. G.; Lord, R. W.; McCormick, C. R.; Domizio, G. A. D.; Schaak, R. E. Experimental Insights into Partial Cation Exchange Reactions for Synthesizing Heterostructured Metal Sulfide Nanocrystals. *Chem. Mater.* **2020**, *32*, 5461–5482. DOI: 10.1021/acs.chemmater.0c01388

- (30) O'Boyle, S. K.; Baumler, K. J.; Schaak, R. E. Unexpected Multi-Step Transformation of AgCuS to AgAuS During Nanoparticle Cation Exchange. *Inorg. Chem.* **2023**, DOI: 10.1021/acs.inorgchem.3c01869
- (31) Mumme, W. G.; Gable, R. W.; Petricek, V. The Crystal Structures of Roxbyite, Cu<sub>58</sub>S<sub>32</sub>. *The Canadian Mineralogist* **2012**, *50*, 423–430. DOI: 10.3749/canmin.50.2.423
- (32) Xu, Y.-N.; Ching, W. Y. Electronic, Optical, and Structural Properties of Some Wurtzite Crystals. *Phys. Rev. B* **1993**, *48*, 4335–4351. DOI: 10.1103/PhysRevB.48.4335
- (33) Zhai, Y.; Shim, M. Effects of Copper Precursor Reactivity on the Shape and Phase of Copper Sulfide Nanocrystals. *Chem. Mater.* **2017**, 29, 2390–2397. DOI: 10.1021/acs.chemmater.7b00461
- (34) Gariano, G.; Lesnyak, V.; Brescia, R.; Bertoni, G.; Dang, Z.; Gaspari, R.; De Trizio, L.; Manna, L. Role of the Crystal Structure in Cation Exchange Reactions Involving Colloidal Cu<sub>2</sub>Se Nanocrystals. *J. Am. Chem. Soc.* **2017**, *139*, 9583–9590. DOI: 10.1021/jacs.7b03706
- (35) Sadtler, B.; Demchenko, D. O.; Zheng, H.; Hughes, S. M.; Merkle, M. G.; Dahmen, U.; Wang, L. W.; Alivisatos, A. P. Selective Facet Reactivity during Cation Exchange in Cadmium Sulfide Nanorods. *J. Am. Chem. Soc.* **2009**, *131*, 5285–5293. DOI: 10.1021/ja809854q
- (36) Fenton, J. L.; Steimle, B. C.; Schaak, R. E. Exploiting Crystallographic Regioselectivity To Engineer Asymmetric Three-Component Colloidal Nanoparticle Isomers Using Partial Cation Exchange Reactions. *J. Am. Chem. Soc.* **2018**, *140*, 6771–6775. DOI: 10.1021/jacs.8b03338
- (37) Miller, T. A.; Wittenberg, J. S.; Wen, H.; Connor, S.; Cui, Y.; Lindenberg, A. M. The mechanism of ultrafast structural switching in superionic copper (I) sulphide nanocrystals. *Nat Commun* **2013**, *4*, 1369. DOI: 10.1038/ncomms2385
- (38) Gong, J.; Jain, P. K. Room-temperature superionic-phase nanocrystals synthesized with a twinned lattice. *Nat Commun* **2019**, *10*, 3285. DOI: 10.1038/s41467-019-11229-2
- (39) Wang, L. W. High Chalcocite Cu<sub>2</sub>S: A Solid-Liquid Hybrid Phase. *Phys. Rev. Lett.* **2012**, 108, 085703. DOI: 10.1103/PhysRevLett.108.085703
- (40) Chakrabarti, D. J.; Laughlin, D. E. The Cu-S (Copper-Sulfur) System. *Bulletin of Alloy Phase Diagrams* **1983**, *4*, 254–271. DOI: 10.1007/BF02868665
- (41) Lu, D.; Xu, X.; Zhang, X.; Xie, W.; Gao, Y. Study on Influencing Factors of Phase Transition Hysteresis in the Phase Change Energy Storage. *Materials* **2022**, *15*, 2775. DOI: 10.3390/ma15082775
- (42) Serikawa, M.; Mabuchi, K.; Satoh, M.; Nozue, Y.; Hayashi, Y.; Yokoyama, M. Measurement of full-scale phase change material products considering hysteresis. *Appl. Therm.Eng.* **2021**, *192*, 116895. DOI: 10.1016/j.applthermaleng.2021.116895
- (43) Mehling, H.; Barreneche, C.; Solé, A.; Cabeza, L. F. The connection between the heat storage capability of PCM as a material property and their performance in real scale applications. *J. Energy Storage* **2017**, *13*, 35–39. DOI: 10.1016/j.est.2017.06.007
- (44) Casu, A.; Genovese, A.; Manna, L.; Longo, P.; Buha, J.; Botton, G. A.; Lazar, S.; Kahaly, M. U.; Schwingenschloegl, U.; Prato, M.; Li, H.; Ghosh, S.; Palazon, F.; De Donato, F.; Lentijo Mozo, S.; Zuddas, E.; Falqui, A. Cu<sub>2</sub>Se and Cu Nanocrystals as Local Sources of Copper in Thermally Activated *In Situ* Cation Exchange. *ACS Nano* **2016**, *10*, 2406–2414. DOI: 10.1021/acsnano.5b07219

- (45) Bonifacio, C. S.; Carenco, S.; Wu, C. H.; House, S. D.; Bluhm, H.; Yang, J. C. Thermal Stability of Core–Shell Nanoparticles: A Combined in Situ Study by XPS and TEM. *Chem. Mater.* **2015**, *27*, 6960–6968. DOI: 10.1021/acs.chemmater.5b01862
- (46) Zheng, H.; Rivest, J. B.; Miller, T. A.; Sadtler, B.; Lindenberg, A.; Toney, M. F.; Wang, L.-W.; Kisielowski, C.; Alivisatos, A. P. Observation of Transient Structural-Transformation Dynamics in a Cu<sub>2</sub>S Nanorod. *Science* **2011**, *333*, 206–209. DOI: 10.1126/science.1204713
- (47) Egerton, R. F.; Li, P.; Malac, M. Radiation Damage in the TEM and SEM. *Micron* **2004**, *35*, 399–409. DOI: 10.1016/j.micron.2004.02.003
- (48) Houk, L. R.; Challa, S. R.; Grayson, B.; Fanson, P.; Datye, A. K. The Definition of "Critical Radius" for a Collection of Nanoparticles Undergoing Ostwald Ripening. *Langmuir* **2009**, 25, 11225–11227. DOI: 10.1021/la902263s
- (49) Dagtepe, P.; Chikan, V. Quantized Ostwald Ripening of Colloidal Nanoparticles. *J. Phys. Chem. C* **2010**, *114*, 16263–16269. DOI: 10.1021/jp105071a
- (50) Gentry, S. T.; Kendra, S. F.; Bezpalko, M. W. Ostwald Ripening in Metallic Nanoparticles: Stochastic Kinetics. *J. Phys. Chem. C* **2011**, *115*, 12736–12741. DOI: 10.1021/jp2009786
- (51) Voorhees, P. W. Ostwald Ripening of Two-Phase Mixtures. Annu. Rev. Mater. Sci. 1992, 22, 197–215. DOI: 10.1146/annurev.ms.22.080192.001213
- (52) Demchenko, D. O.; Robinson, R. D.; Sadtler, B.; Erdonmez, C. K.; Alivisatos, A. P.; Wang, L. W. Formation Mechanism and Properties of CdS-Ag<sub>2</sub>S Nanorod Superlattices. *ACS Nano* **2008**, *2*, 627–636. DOI: 10.1021/nn700381y

**Table of Contents Graphic** 

